crystals

MDPI

Article

Rapid Microwave Method for Synthesis of Iron Oxide Particles under Specific Conditions

Ivana Mitar [1,*], Lucija Guć [2], Željka Soldin [3], Martina Vrankić [4], Andrea Paut [5], Ante Prkić [5] and Stjepko Krehula [6]

1 Faculty of Science, University of Split, Ruđera Boškovića 33, 21000 Split, Croatia
2 University of Split, Ruđera Boškovića 31, 21000 Split, Croatia; lucija.guc95@gmail.com
3 Department of Chemistry, Faculty of Science, University of Zagreb, Horvatovac 102a, 10000 Zagreb, Croatia; zeljka@chem.pmf.hr
4 Division of Materials Physics and Center of Excellence for Advanced Materials and Sensing Devices, Ruđer Bošković Institute, Bijenička 54, 10000 Zagreb, Croatia; martina.vrankic@irb.hr
5 Faculty of Chemistry and Technology, University of Split, Ruđera Boškovića 35, 21000 Split, Croatia; andrea.paut@ktf-split.hr (A.P.); prkic@ktf-split.hr (A.P.)
6 Division of Materials Chemistry, Ruđer Bošković Institute, Bijenička 54, 10000 Zagreb, Croatia; krehul@irb.hr
* Correspondence: imitar@pmfst.hr; Tel.: +385-21-691-279

Abstract: The advantages of microwave technology over conventionally conducted experiments are numerous. Some of them are reduction in reaction time, a higher degree of process control, repeatability, and work safety. Microwave synthesis routes require a complete description of the experimental details, instrumentation, and design program of a microwave oven used in the experiments. In this work, microwave-assisted hydrothermal synthesis of hematite (α-Fe_2O_3) particles from 0.1 M $FeCl_3$ solution in highly alkaline media with heating in a microwave oven at continuous microwave emission of 800 W at 150 °C, 200 °C, and 250 °C for 20 min are presented. Also, the influence of the percentage of the addition of a cationic surfactant, cetyltrimethylammonium bromide (CTAB) on the composition, size, and shape of the final product was investigated. The samples precipitated at 150 °C formed a final product consisting of goethite (α-FeOOH) and hematite particles in contrast to the those precipitated at 200 °C and 250 °C where pure hematite phase was obtained. In these synthesis routes, the CTAB caused to slow down the rate of the goethite-to-hematite transformation process at temperatures at 200 °C but did not affect the transformation at 250 °C.

Keywords: microwave-assisted synthesis; hematite; α-Fe_2O_3 particles; goethite; α-FeOOH particles; cetyltrimethylammonium bromide; FT-IR spectroscopy; powder X-ray diffraction; FE-SEM

Citation: Mitar, I.; Guć, L.; Soldin, Ž.; Vrankić, M.; Paut, A.; Prkić, A.; Krehula, S. Rapid Microwave Method for Synthesis of Iron Oxide Particles under Specific Conditions. *Crystals* **2021**, *11*, 383. https://doi.org/10.3390/cryst11040383

Academic Editors: Boris-Marko Kukovec and Martin Dressel

Received: 13 February 2021
Accepted: 2 April 2021
Published: 6 April 2021

1. Introduction

During the last decades, microwaves have been studied as a source of energy for chemical reactions and processes, mainly for organic synthesis pathways rather than inorganic ones. Although the number of papers dealing with the microwave-assisted synthesis of inorganic nanomaterials has been extensive since the 1990s in all classes of functional materials such as metals, oxides, sulfides, phosphates, and halides, microwave synthesis is not yet where it belongs in science [1]. Advantages of microwave technology over conventionally performed experiments are numerous and well known. Some of them are reducing reaction times and energy costs, suppression of side reactions and, hence, improvement in product yield, purity, better material properties, a higher degree of process control, repeatability, and safety [1,2]. All advantages of microwave technology can be attributed to the efficient internal heating (in-core volumetric heating) by direct coupling of microwave energy with the molecules (solvents, reagents, catalysts) so that the temperature rise is uniform throughout the sample [3].

In many publications, the microwave systems used are usually insufficiently described and details regarding the experimental conditions are relatively scarce. Essential reaction

parameters, such as the power used in the experiments or the temperatures reached, are not given, which is mainly due to the use of domestic microwave ovens. Namely, a domestic microwave oven cannot provide the required information because the irradiation power is controlled by on–off cycles of the magnetron. Therefore, it is not possible to reliably monitor the reaction temperature. Many published papers describe only "full power" or 2.45-GHz power specifications, and very few published synthesis routes can be repeated. There are no literature data on the repeatability of synthesis products prepared using microwave techniques. Reactions carried out in this way cannot be compared with literature data, so such procedures cannot be recommended for scientific purposes, nor can they guarantee the safety of the work. Schütz et al. discussed the difficulty of direct comparison of conditions performed by microwave-assisted synthesis methods [4]. Microwave synthesis routes require a detailed description of the experimental procedure, such as the apparatus, reaction protocol, instrumentation, and design program of a microwave oven used in experiments. The only disadvantage of microwave technology is the high capital cost of professional chemical microwave systems. Modern professional microwave reactors allow autoclave process conditions of 300 °C and 100 bar under carefully controlled and safe operating conditions, with the continuous rotation of samples within the cavity and the possibility of mixing samples within a reaction vessel [2]. These systems allow temperature measurements directly in the microwave field by IR sensors or in the reaction mixture using fiber optic sensors and software that enable temperature control by regulating the microwave power with faster temperature rise and cooling [5].

Iron oxyhydroxides and oxides are widely spread in our environment, while synthetic iron oxides are heavily used in advanced technologies. For this reason, the synthesis of iron oxides is a well-investigated scientific topic. Hematite (α-Fe_2O_3) and goethite (α-FeOOH) are the most studied materials due to their diverse applications in many scientific and industrial fields, e.g., as inorganic pigments [6,7]; adsorbents for wastewater treatment [8,9]; abrasives [10]; gas sensors; catalysts [11]; electrochemical sensors [12,13]; and precursors in the manufacture of electronic, magnetic, or optical devices and medical diagnosis or therapy [10,14–17]. The chemical composition, purity, morphology, and size of iron oxide particles are the key features for their application. Each potential application requires different properties of the particles, for example, a stable, switchable, magnetic state of iron oxide particles is necessary for data storage applications, while the stability in the water at pH 7 is crucial for the versatile biomedical applications [16]. The properties of iron oxide particles mainly depend on the preparation method and experimental conditions of the synthesis route. Due to the use of iron oxides in advanced technologies and because they are non-toxic, biocompatible, and cheap to produce, scientists and engineers have investigated various methods for the synthesis of precisely defined iron oxide nano/microstructures. However, designing the iron oxide particles of defined size and morphology for targeted applications is still a major research challenge. In their book, Yue et al. highlighted the great challenge of how to efficiently synthesize iron oxides with controlled morphology, size, and functionality and how to fundamentally understand the formation, growth mechanisms, and structure of iron oxide particles [18]. Machala et al., in their review paper, described parameters affecting polymorphous transformations of iron oxides, which is a great challenge in the study of polymorphism of solid compounds [19].

Among the many available and widely studied methods for the synthesis of hematite and goethite particles (e.g., sol-gel, microemulsion method, thermal decomposition, sono-chemical techniques), hydrothermal techniques were the fastest, easiest, and most widely used pathways for the preparation of these oxides. The hydrothermal routes under different experimental conditions of pressure, temperature, pH medium, reaction time, precursor type, and concentration are well investigated and reported in the literature [6,10,11,14,20–46].

As mentioned earlier, microwave-assisted hydrothermal techniques are still not well investigated because of the high capital cost of professional chemical microwave systems. There are many published papers in the literature describing the microwave-assisted hydrothermal synthesis of iron oxide particles prepared using a domestic microwave oven,

without specifying microwave instrumentation and experimental conditions [12,47–53] or using microwave digestion systems, where the temperature reached is calculated by the temperature/pressure ratio based on the steam tables [47,51–60]. Few published papers described program details of a professional microwave oven, thus providing specific and well-established experimental conditions that could ensure reproducibility [50,56,61–64].

In recent years, the influence of added polysaccharides [65,66], surface-active substances [42,67–73], soluble polymers, and biopolymers [18,20,44,72,74–76] was intensively studied under the influence of various experimental factors in the abovementioned synthesis for iron oxide nano/microstructures. The role of various additives in the synthesis of iron oxide fascinates scientists because of the impact on the morphology of particles: both on the internal properties of particles and the external parameters (e.g., particle morphology, degree of particle aggregation, the size distribution of particles) and polymorphous transformation pathways. Commonly, the additives are used in synthesis as a coating material for particles to design their specific properties for targeted applications [45]. Cole et al. showed the application and advantages of coated iron nanoparticles for magnetic tumor targeting [77]. Kumagai et al. [78] described a simple route for the synthesis of polyethylene glycol (PEG)-coated iron oxide nanoparticles featuring excellent solubility and stability in an aqueous solution.

Microwave-assisted hydrothermal synthesis ensures rapid research of the influence of various additives and their added amount in the synthesis mixture. In 2007, Zhu and co-workers reported the microwave synthesis of Fe_3O_4 nanoparticles and ellipsoidal Fe_2O_3 nanoparticles with a nonionic surfactant, PEG [47]. Yang et al. published the microwave synthesis of spherical nanoporous Fe_3O_4 nanoparticles, also with PEG [79]. Unfortunately, none of the mentioned papers provided microwave instrument-specific experimental conditions that can be easily replicated. Finding a microwave synthesis route that is fast and repeatable could ensure that future studies change only one variable in the synthesis route and examine its effects on the final product.

In this work, the microwave-assisted hydrothermal synthesis of the α-Fe_2O_3 and α-FeOOH was carried out in a highly alkaline medium using $FeCl_3$ precursor. The influence of the added amount of cationic surfactant, cetyltrimethylammonium bromide (CTAB), was investigated. Iron oxide particles synthesized under the specified experimental conditions were in excellent agreement with the literature data. It was found that the control of the experimental conditions can be performed effortlessly and rapidly using a professional microwave oven.

2. Materials and Methods

2.1. Materials

All the required solutions were prepared by dissolving a certain amount of chemicals in ultrapure water. Ultrapure water (declared conductivity of 0.04 μS cm^{-1}) was prepared using the ultrapure water purification system Millipore Simplicity 185, Burlington, MA, USA; resistivity at 25 °C was 18.2 MΩ cm^{-1}.

The following chemicals were used: $FeCl_3 \cdot 6H_2O$ in reagent grade, NaOH (Kemika, Croatia), and cetyltrimethylammonium bromide, CTAB (Alfa Aesar, Ward Hill, MA, USA). Absolute alcohol, pro analysis pure, and 25% ammonium supplied by Gram-mol, Zagreb, Croatia.

2.2. Synthesis

Precipitation experiments were performed at room temperature (RT) in alkali-resistant plastic bottles to avoid contamination by dissolved silicon from glassware. All mixtures were prepared by adding 4 mL of 1 M $FeCl_3$ solution, 32 mL of water, and 4 mL of 8M NaOH solution. For the samples that contained the addition of CTAB, different masses of CTAB were added. After vigorous shaking of each precipitation mixture, the suspension was transferred to a Milestone Teflon-lined, non-stirred pressure vessel. The samples were heated for 20 min in a microwave oven (Milestone, FlexiWave SK15, Sorisole (Bergamo),

Italy, direct temperature control monitor via microwave-transparent fiber optic sensor up to 300 °C, magnetron frequency 2450 MHz, magnetron output 2 × 950 Watt, power supply 230 V, 50–60 Hz) at the prevailing temperature according to a microwave oven program with rotor twist on and continuous microwave emission at 800 W.

Immediately after the reaction time was completed, the autoclaves were cooled utilizing a cooling program of the microwave oven and left inside until the final temperature in the vessels was 25 °C. The mother liquor was separated from the precipitate using the ultrafast centrifuge (Beckman Avanti J-25, Indianapolis, IN, USA). The pH of the mother liquor was measured using a pH meter Mettler Toledo, MP220, Columbus, OH, USA. The precipitates were additionally washed with ultrapure water and ethanol to remove the "neutral" electrolyte and dried in a vacuum oven, Thermo Scientific, 3608–1CE, Waltham, MA, USA at 60 °C overnight.

2.3. FT-IR Spectroscopy

A Shimadzu IR Prestige-21, FTIR-8400S spectrophotometer, Kyoto, Japan, was used to collect the FT-IR spectra. Prior to the analysis, the samples were mixed with spectroscopically pure KBr (Alfa Aesar, Ward Hill, MA, USA) and pressed into pellets. All spectra were processed by the Origin program [80].

2.4. Powder X-ray Diffraction

Powder X-ray diffraction (PXRD) patterns were collected using a *Malvern Panalytical Aeris* XRD diffractometer with CuKα (λ = 1.5406 Å) radiation, Ni filter, and solid-state PIXcel3D-Medipix3 detector. The data were collected in the 2θ range from 15° to 90° with a step size of 0.022°, scan rate 39.53 s/°, $\frac{1}{4}$-inch divergence slit, and 13-mm beam mask. The detector energy discrimination levels were adjusted to suppress the sample fluorescence. The estimated mass fractions of the identified phases [81] were calculated by the Rietveld algorithm [82] using the X'Pert HighScore Plus program [83]. A pseudo-Voigt profile function and a polynomial background model were applied in the structure refinements, whereas the isotropic vibration modes were assumed for all atoms. The crystallite sizes in samples were calculated using the phase fit method (i.e., simultaneously with the Rietveld refinements) based on the change of the profile widths, compared to a standard sample.

2.5. Field-Emission Scanning Electron Microscopy

The morphology of samples was studied using a thermal field-emission scanning electron microscope (FE-SEM) JEOL JSM-7000F, Tokyo, Japan.

3. Results

The experimental conditions for the preparation of the reference samples and samples prepared in the presence of the surfactant CTAB are shown in Table 1. The samples were prepared at different temperatures with the same aging time, 20 min.

Table 1. Experimental conditions for iron oxide particles' preparation.

Sample	1 M $FeCl_3$ /mL	H_2O /mL	8M NaOH /mL	CTAB * /g	CTAB * /%	T/°C	t/min	pH
RS1	4	32	4			150	20	13.39
RS2	4	32	4			200	20	13.51
RS3	4	32	4			250	20	13.35
S1	4	32	4	0.4	1	150	20	13.39
S4	4	32	4	0.1	0.25	200	20	13.16
S5	4	32	4	0.2	0.5	200	20	13.11
S2	4	32	4	0.4	1	200	20	13.46
S6	4	32	4	1.0	2.5	200	20	13.35
S3	4	32	4	0.4	1	250	20	13.38
S7	4	32	4	1.0	2.5	250	20	13.28

* CTAB (cetyltrimethylammonium bromide).

3.1. Fourier-Transform Infrared Spectroscopy Features and Structural Characterization

The FT-IR spectra of selected reference samples and samples with the addition of 1% CTAB in the precipitation mixture are shown in Figure 1.

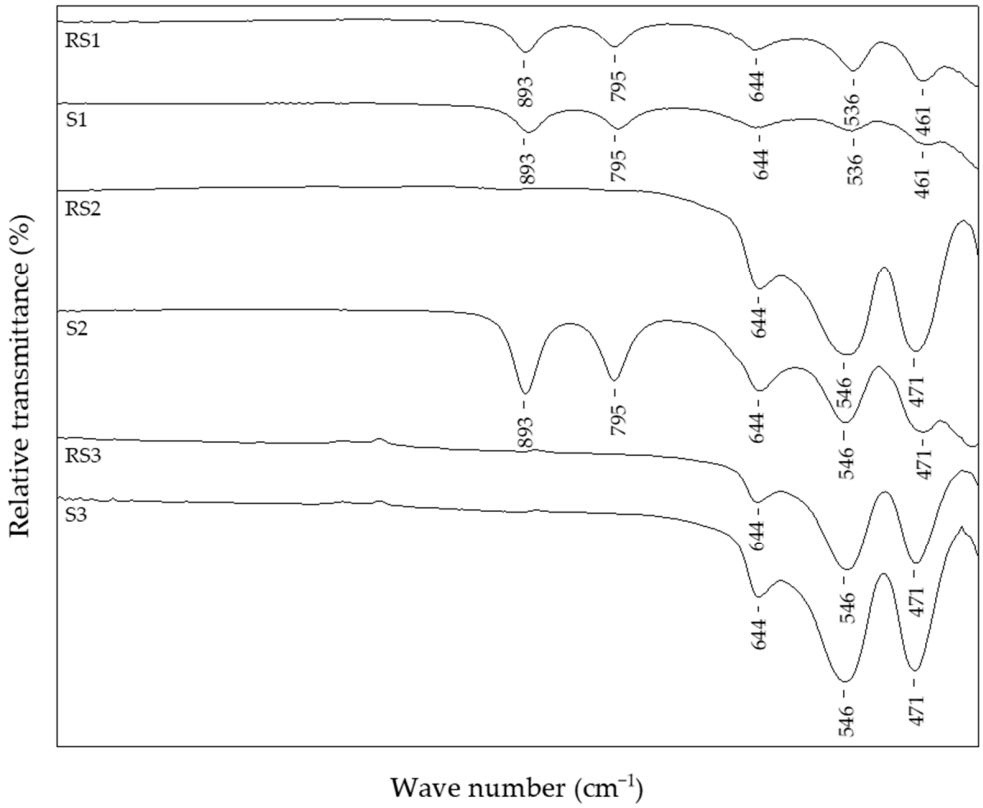

Figure 1. FT-IR spectra of reference samples and samples with 1% CTAB.

The reference sample RS1 and sample S1 with 1% CTAB, prepared at 150 °C, showed the same IR bands typical of goethite and hematite. The in-plane bending band (δOH), positioned at 893 cm^{-1}, and out-of-plane band (γOH), positioned at 795 cm^{-1}, are typically IR bands characteristic for α-FeOOH. The IR band recorded at 644 cm^{-1} presented the low-wave lattice mode of FeO_6 and its position was influenced by the particle shape [84] or could be related to the interaction of Fe-OH groups with Cl^- ions [34]. On the other hand, the IR bands at 536 and 461 cm^{-1} indicated an α-Fe_2O_3 phase. As the IR active vibrations of hematite are dependent on optical parameters and geometric shape [85], the shift of the IR band at ~536 cm^{-1} might have been due to the different geometric shapes of hematite particles in these samples.

The results of the semi-quantitative phase analysis based on Hill and Howard formalism [86] along with the refined unit cell parameters are compiled in Table 2.

Table 2. Results of semi-quantitative phase analysis as obtained from Rietveld refinement against PXRD data at RT (λ = 1.5406 Å). R_{wp} is the discrepancy factor that characterizes the quality of the fit [87]. Standard deviations are given in parentheses.

Sample	Unit Cell Metrics					Phase Fraction (wt.%)	R_{wp} (%)
	α-Fe_2O_3 (s.g. *R*-3c)		α-FeOOH (s.g. *P*bnm)				
	a (Å)	*c* (Å)	*a* (Å)	*b* (Å)	*c* (Å)		
RS1	5.034 (2)	13.748 (1)	9.954 (6)	3.020 (4)	4.606 (5)	40.8 59.2	8.93
S1	5.0321 (3)	13.741 (1)	9.950 (1)	3.020 (4)	4.6049 (6)	20.6 79.4	7.47
RS2	5.025 (1)	13.725 (9)				100	8.97
S2	5.031 (2)	13.7397 (5)	9.949 (9)	3.0193 (2)	4.6016 (3)	41.1 58.9	7.35
S4	5.031 (1)	13.7397 (5)	9.956 (6)	3.018 (1)	4.598 (1)	89.7 10.3	8.26
S5	5.031 (3)	13.7388 (9)	9.950 (2)	3.0182 (5)	4.5994 (6)	52.2 47.8	7.24
S6	5.0325 (1)	13.749 (5)	9.957 (1)	3.0204 (3)	4.6040 (4)	39.5 60.5	6.89
S7	5.0416 (1)	13.766 (5)				100	9.33
RS3	5.0355 (1)	13.754 (4)				100	6.72
S3	5.0367 (4)	13.757 (1)				100	6.69

PXRD patterns of the samples RS1 and S1 indicated a presence of orthorhombic, goethite assembly (space group *P*bnm) and rhombohedral, hematite phase (space group *R*-3c) (Figure 2). However, the sample S2, with 1% CTAB addition, differed from sample RS2 prepared at the same temperature, 200 °C. Namely, the FT-IR spectra of sample RS2 (Figure 1) and PXRD patterns (Figure 3) indicated the formation of solely hematite phase. As opposed to that, the FT-IR spectra of sample S2 (Figure 1) showed IR bands that can be assigned to both goethite phase (IR bands at 893 and 795 cm^{-1}) and hematite phase (IR bands at 546 and 471 cm^{-1}). The mixture of both Fe phases in sample S2 was evidenced by the collected PXRD patterns (Figure 3). Reference sample RS3 and sample S3 prepared at 250 °C did not show IR bands at 893 cm^{-1} or 795 cm^{-1}, but very intense hematite bands were observed at 546 and 471 cm^{-1} (Figure 1). From the IR spectra and the PXRD pattern (Figure 4), the presence of hematite as a single phase was evident in the reference sample RS3 and sample with 1% CTAB addition, S3. The samples RS1 and S1, synthesized at 150 °C, differed in their composition ratio. Namely, the reference sample RS1 contained ~40 wt.% α-Fe_2O_3 and ~60 wt.% α-FeOOH, while sample S1, with 1% CTAB, contained ~20 wt.% α-Fe_2O_3 and ~80 wt.% α-FeOOH. Sample RS2, prepared at 200 °C, contained solely α-Fe_2O_3 and sample S2, made at the same experimental conditions as RS2 but with 1% of CTAB addition, contained ~40 wt.% of α-Fe_2O_3 and ~60 wt.% of α-FeOOH phase (Figure 3). Reference sample RS3 and sample S3, prepared at 250 °C, contained only the hematite phase (Figure 4). A similar trend was observed in sample S7, with 2.5% of CTAB. No impurities were detected in those samples. The values of crystallite sizes obtained from the line-broadening analysis during the crystal structure refinements were in the range between 24.6(1) and 81.0(1) for the α-Fe_2O_3 phase and 21.2(1) and 36.7(1) for the α-FeOOH (Table 3).

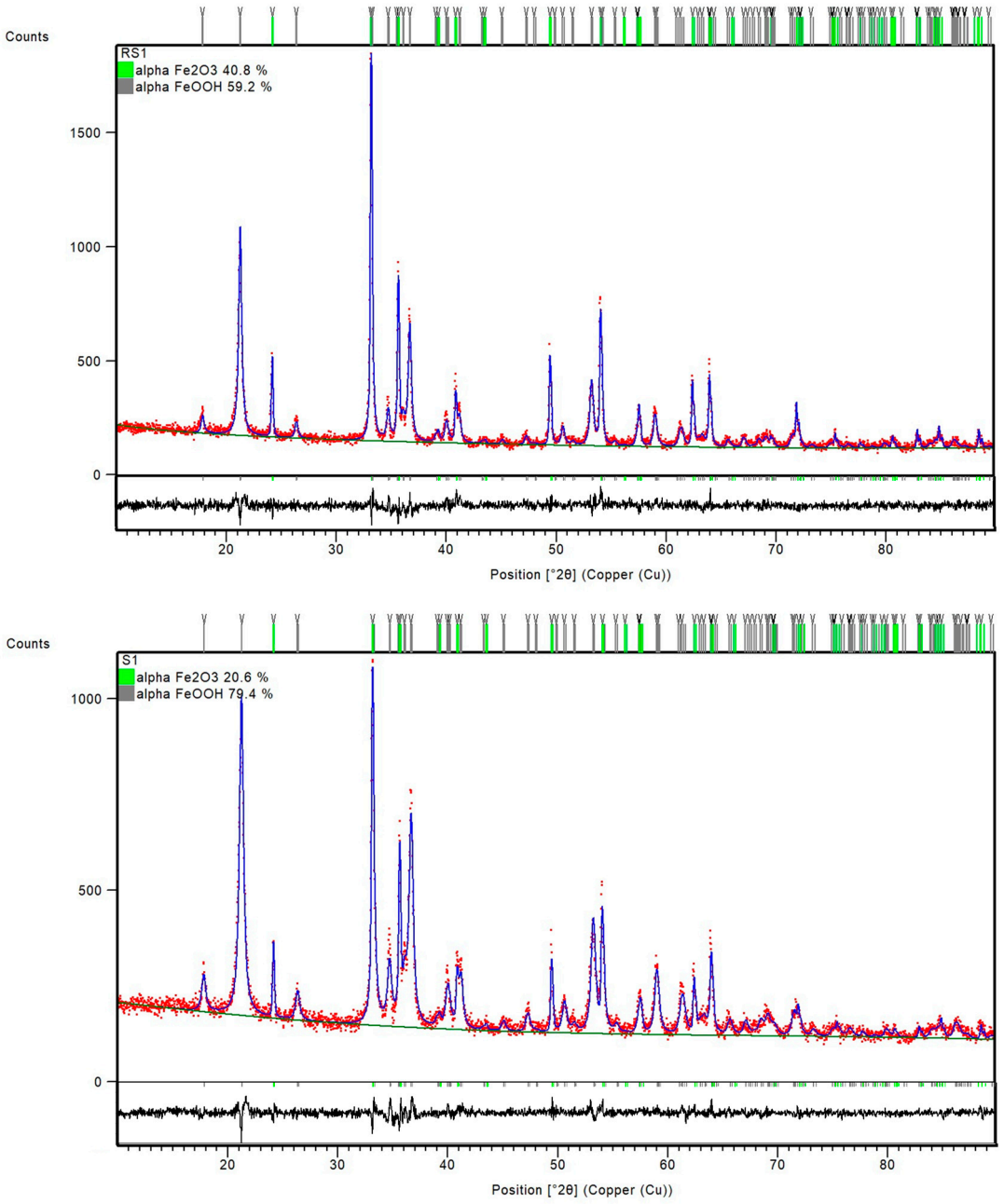

Figure 2. Final observed (red dots) and calculated (blue, solid lines) powder diffraction profiles for reference sample RS1 and sample S1 as obtained from the Rietveld refinement. The green and gray tick marks show the reflection positions of α-Fe_2O_3 and α-FeOOH, respectively. The lower, black, solid lines show the difference profiles.

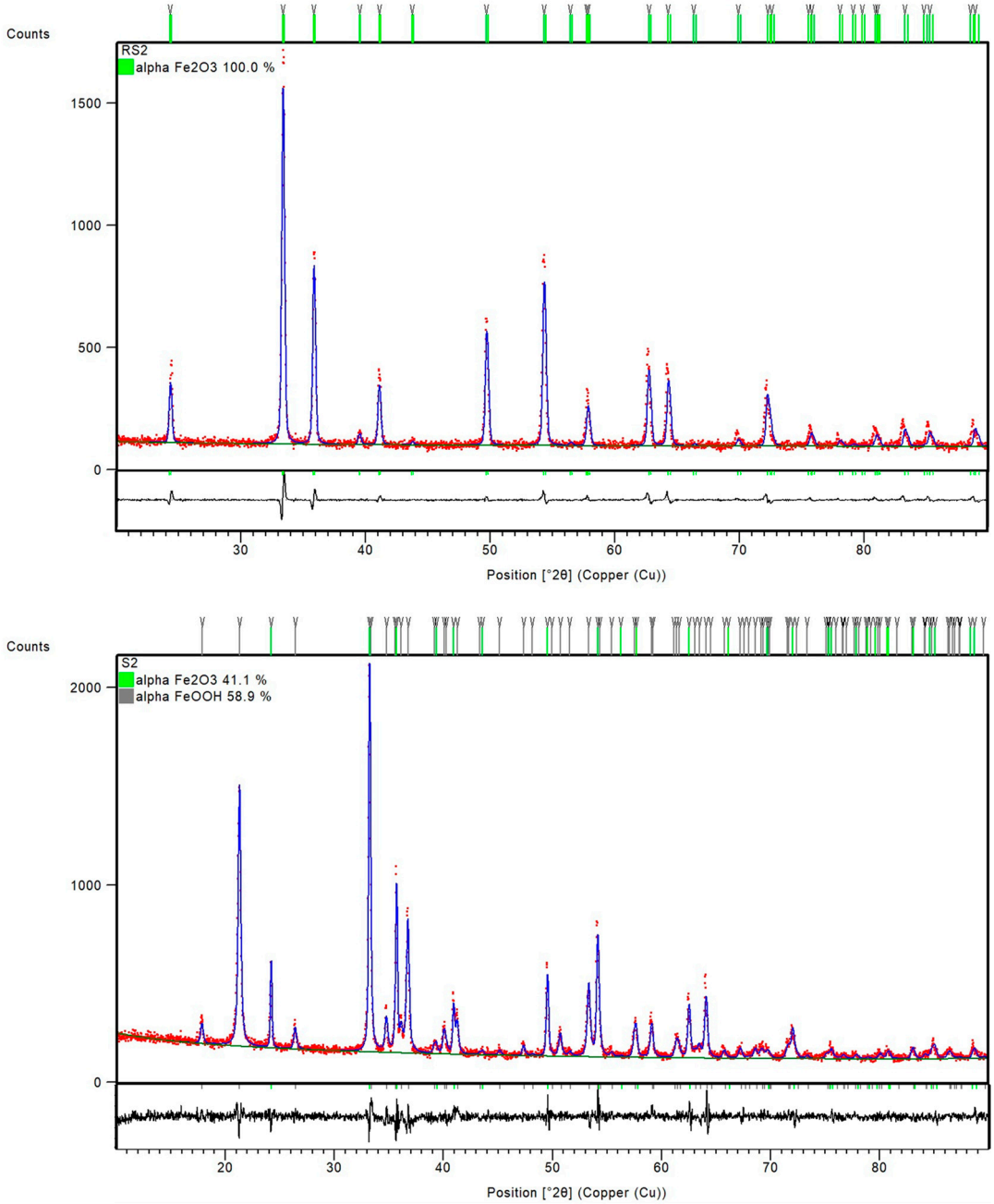

Figure 3. Final observed (red dots) and calculated (blue, solid lines) powder diffraction profiles for reference sample RS2 and sample S2 as obtained from the Rietveld refinement. The green and gray tick marks show the reflection positions of α-Fe_2O_3 and α-FeOOH, respectively. The lower, black, solid lines show the difference profiles.

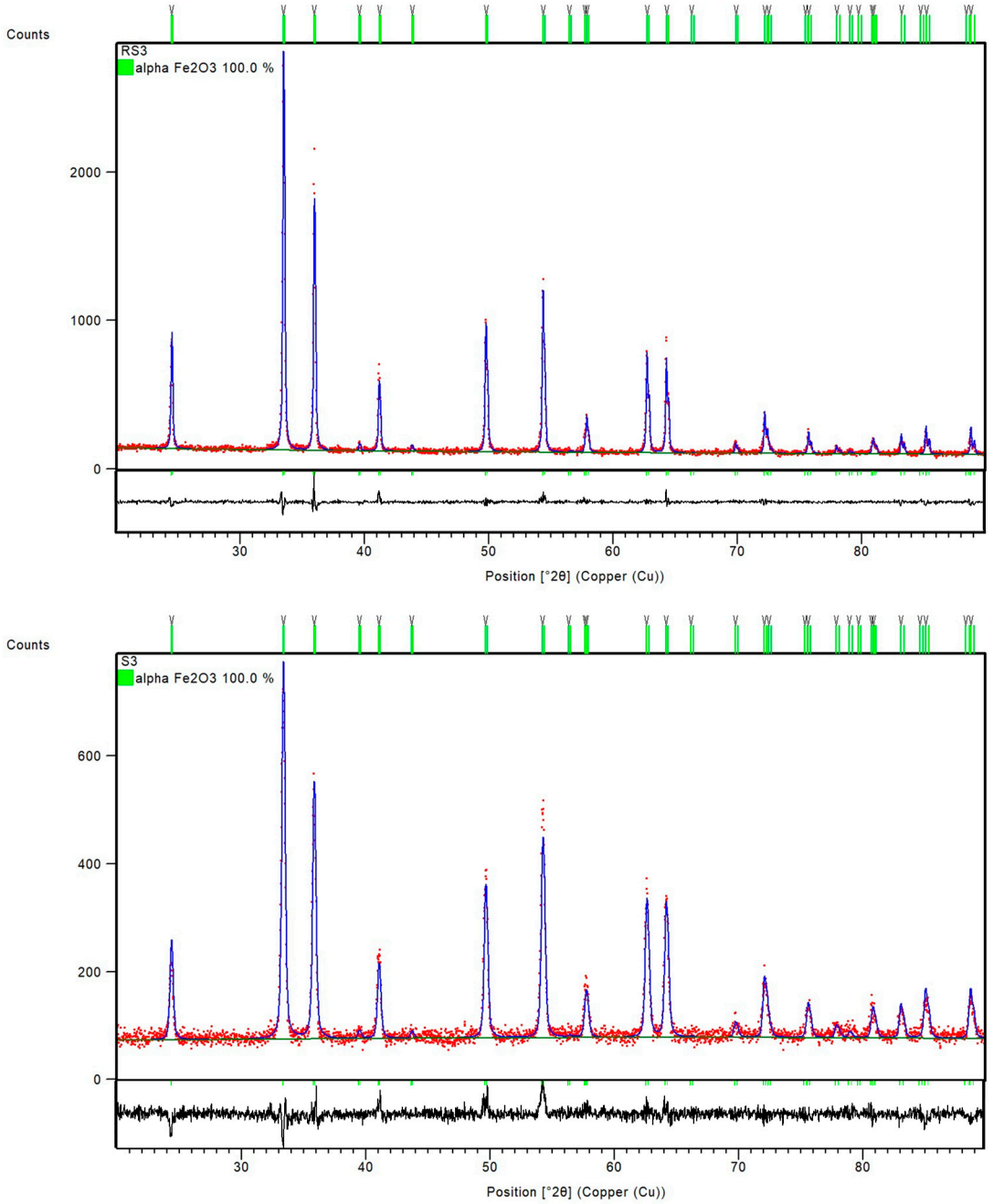

Figure 4. Final observed (red dots) and calculated (blue, solid lines) powder diffraction profiles for reference sample RS3 and sample S3 as obtained from the Rietveld refinement. The green and gray tick marks show the reflection positions of α-Fe_2O_3 and α-FeOOH, respectively. The lower, black, solid lines show the difference profiles.

Table 3. Results of crystallite size calculation as obtained from the phase refinements to PXRD data.

Sample	Crystallite Size (nm)		Phase Fraction (wt.%)
	α-Fe_2O_3 (s.g. *R*-3c)	α-FeOOH (s.g. *P*bnm)	
RS1	66.2 (1)	29.7 (1)	40.8 59.2
S1	63.7 (1)	21.2 (1)	20.6 79.4
RS2	39.5 (1)		100
S2	65.7 (1)	36.7 (1)	41.1 58.9
S4	42.3 (1)	35.5 (1)	89.7 10.3
S5	38.7 (1)	26.4 (1)	52.2 47.8
S6	38.8 (1)	27.7 (1)	39.5 60.5
S7	24.6 (1)		100
RS3	81.0 (1)		100
S3	29.8 (1)		100

Figure 5 shows samples precipitated at 200 °C for 20 min, but with different additions of CTAB in the precipitation system: reference sample, RS2, without CTAB addition; sample S4 with 0.25% of CTAB addition; sample S6 with 2.5% of CTAB added in precipitation mixture. In these experimental conditions, without the CTAB addition, the final product comprised pure hematite phase, as evidenced from the IR spectra of reference sample RS2. Samples with the addition of CTAB (>0.5%) showed no difference according to FT-IR analysis and had the same IR bands positioned at 893 cm^{-1}, 795 cm^{-1}, 644 cm^{-1}, 546 cm^{-1}, 471 cm^{-1}, and 411 cm^{-1} of similar intensity, characteristic for the mixture of hematite and goethite phases. Sample S4, with the smallest amount of CTAB (0.25%), showed the same IR bands but reduced in intensity. Sample S4 contained the largest proportion of hematite, ~90 wt.%, of the final product. On the contrary, the sample S6, with the highest content of CTAB, comprised the smallest fraction of hematite, only 39.5 wt.%, of the final product (Table 2). Figure 6 shows a comparison of IR and the PXRD data of the reference sample RS3, synthesized at 250 °C, and the sample with 2.5% CTAB added to the precipitation mixture, S7, indicating the formation of pure hematite phases.

3.2. Surface Morphology Imaging

FE-SEM image of reference sample RS1 (Figure 7a) shows the presence of nanorods typical of goethite and irregular particles typical of hematite formed at high pH [22]. In the presence of CTAB (sample S1, Figure 7b), an increased fraction of goethite nanorods and smaller hematite irregular particles were visible. FE-SEM image of reference sample RS2 (Figure 7c) shows only the presence of irregular hematite particles, while in the FE-SEM image of sample S2 (Figure 7d) goethite nanorods are also visible.

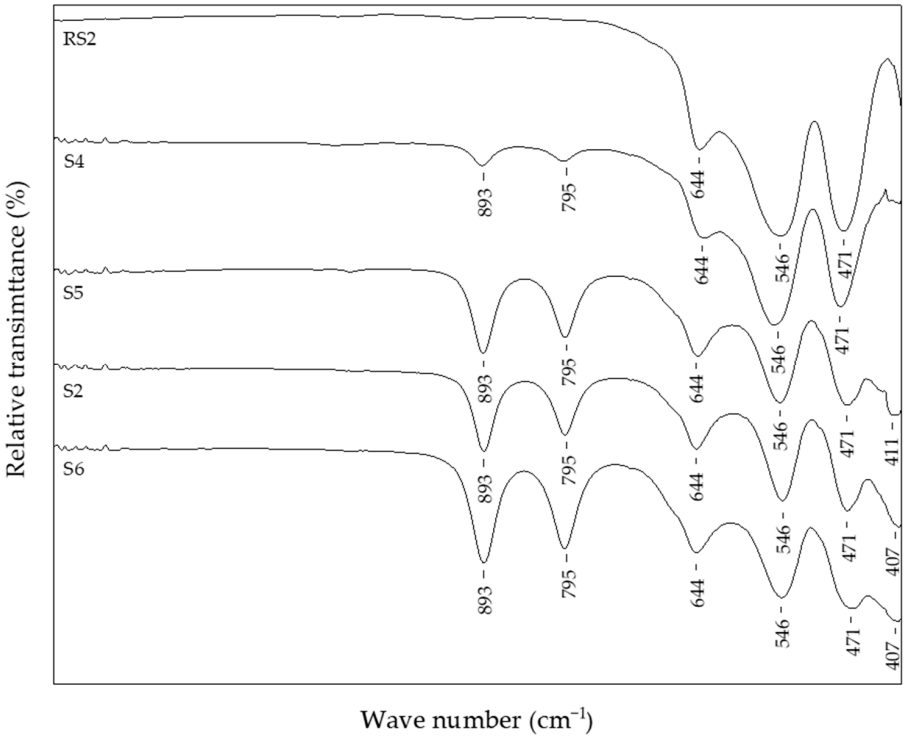

Figure 5. FT-IR spectra of samples with different percentages of CTAB in precipitation mixture.

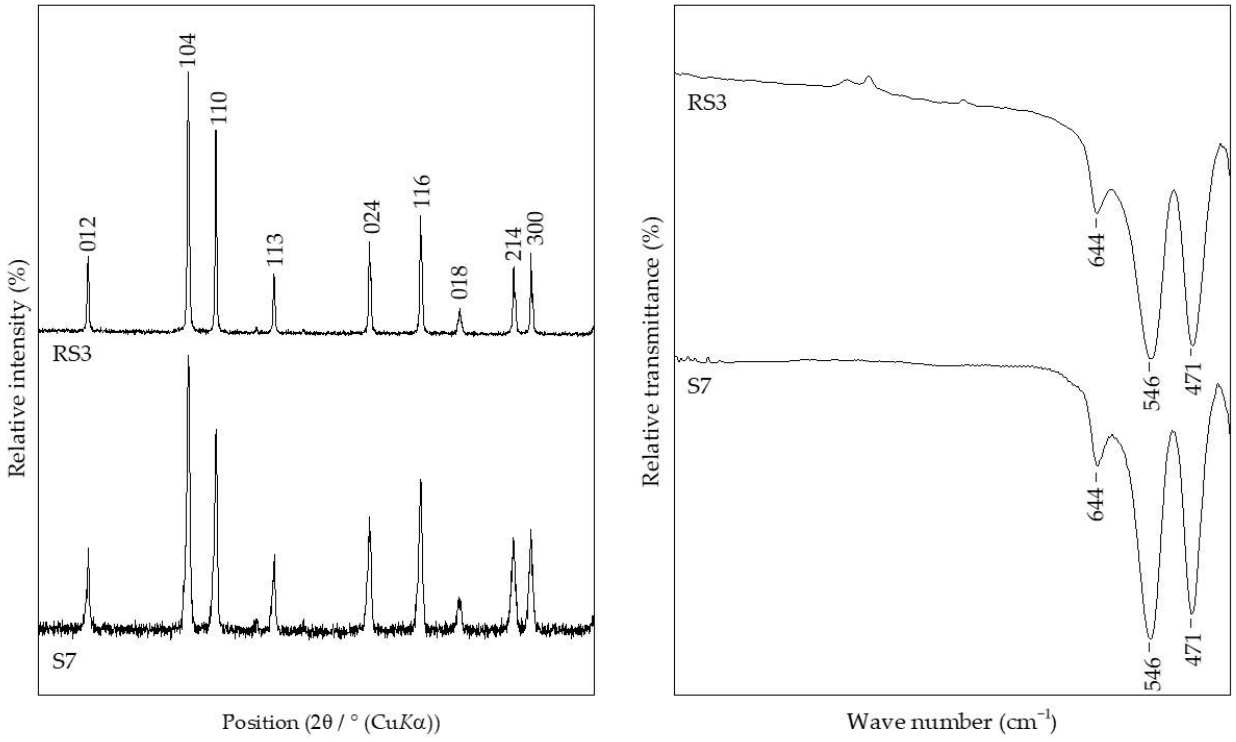

Figure 6. Comparison of PXRD patterns and FT-IR spectra of samples RS3 and S7.

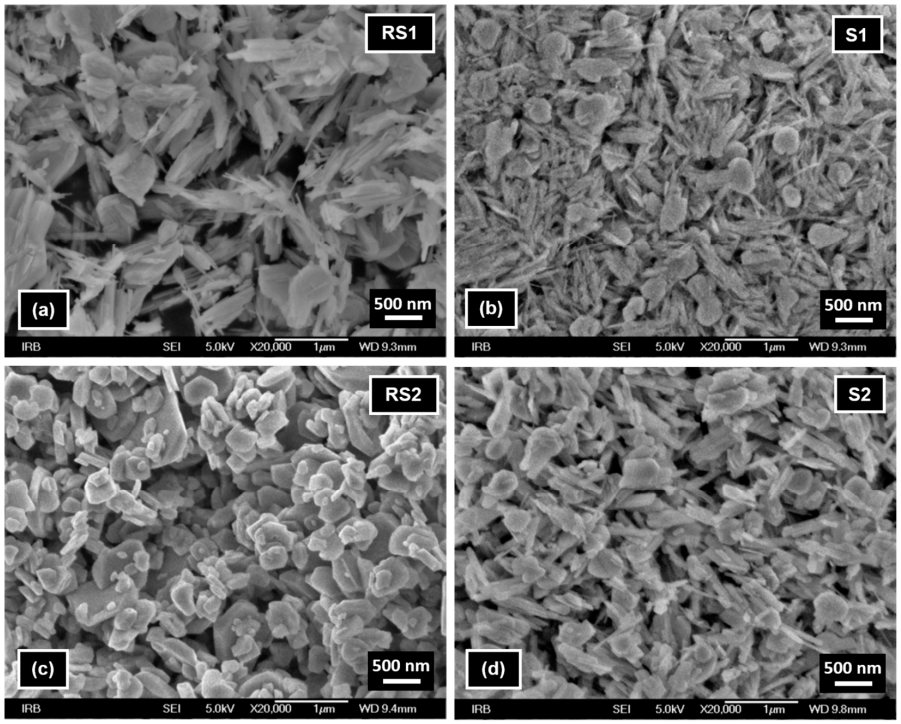

Figure 7. FE-SEM images of samples (**a**) RS1, (**b**) S1, (**c**) RS2, and (**d**) S2 recorded at magnification of 20,000×.

FE-SEM images of reference sample RS3 (Figure 8a) and samples S3 and S7 (Figure 8b–d) show the presence of similar irregular hematite particles of about several tens of nm to 1 μm in size. These images indicate an insignificant influence of the presence of CTAB during high-temperature (250 °C) synthesis on the size and shape of hematite particles.

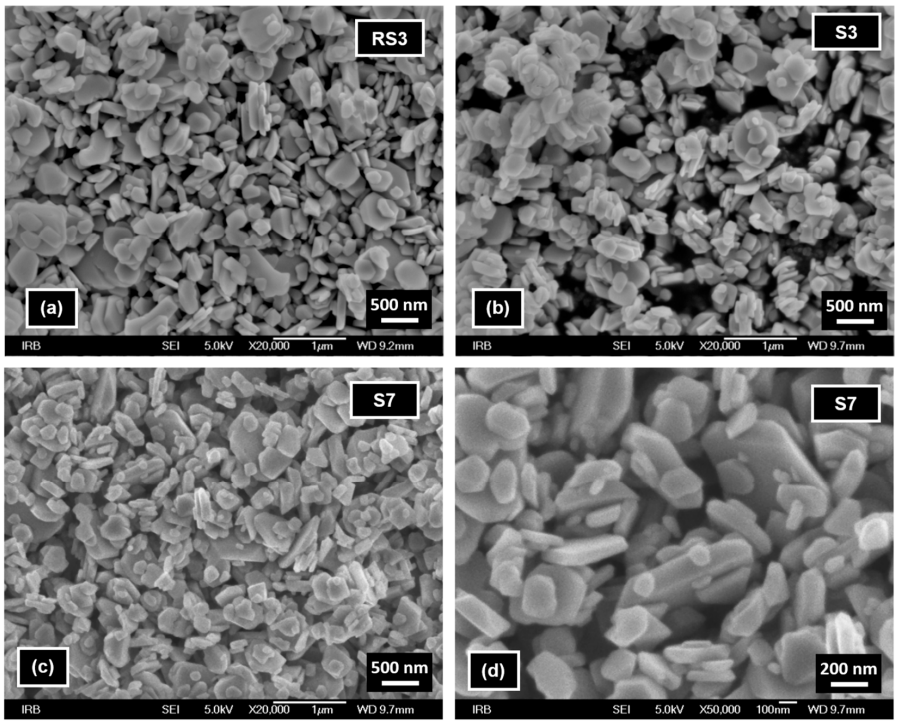

Figure 8. FE-SEM images of samples (**a**) RS3, (**b**) S3, and (**c**) S7 recorded at a magnification of 20,000×, and (**d**) sample S7 recorded at a magnification of 50,000×.

4. Discussion

The formation of α-Fe_2O_3 particles obtained by the precipitation from $FeCl_3$ solution by forced hydrolysis at elevated temperatures dissolved α-FeOOH particles and recrystallizes α-Fe_2O_3 particles, as reported in the literature [22,25,34]. The syntheses reported in these papers represent conventional hydrothermal routes in a gravity furnace under extended reaction time, hours or days. Foreign species in precipitation mixtures for iron oxide synthesis (i.e., anions, cations, or neutral molecules) can have two different effects: They can change either the composition ratio of the final product (goethite/hematite) or they can modify the properties of the final product [6]. The effect of the surfactant CTAB on particle morphology has been studied in previous work using conventional hydrothermal routes under extended reaction time [70].

In this work, we investigated a microwave-assisted hydrothermal accelerated synthesis of α-Fe_2O_3 and α-FeOOH particles from $FeCl_3$ solution in a highly alkaline medium at 150 °C, 200 °C, and 250 °C and 20-min reaction time. The effect of the percentage of a cationic surfactant, CTAB, on the composition, size, and shape of the final product was elaborated in detail.

Reference samples RS1–RS3 and samples S1–S3 were prepared as precipitated mixtures of 0.1 M $FeCl_3$ solution at pH values ~13 and heated at 150 °C, 200 °C, and 250 °C for 20 min in a microwave oven. Samples S1–S3 in the precipitated mixtures contained 1% CTAB. Reference sample RS1 and sample S1 prepared at 150 °C showed the same IR bands, assigned to the formation of goethite and hematite phases. The PXRD patterns in Figure 2 showed the mixture of α-Fe_2O_3 and α-FeOOH in both the reference sample RS1 and sample S1. According to the results of structure refinements, the reference sample RS1 and sample S1 differed in their composition ratio: The sample RS1 contained ~40 wt.% α-Fe_2O_3 and ~60 wt.% α-FeOOH, whereas the sample S1 comprised 20 wt.% α-Fe_2O_3 and 80 wt.% α-FeOOH. Therefore, it can be concluded that CTAB in sample S1 slowed down the rate of the goethite-to-hematite transformation process. A complete transformation of goethite to hematite phase was possible only at higher temperatures. In particular, under hydrothermal conditions, above 150 °C, the formation of the hematite phase was very fast [6]. The FT-IR spectra of the reference sample RS2 in Figure 1 and the PXRD patterns in Figure 3 showed the formation of single-phase α-Fe_2O_3 after 20 min at 200 °C. On the contrary, the sample S2, prepared with the same aging time and temperature as the reference sample RS2 but with 1% CTAB addition, comprised the mixture of both α-Fe_2O_3 and α-FeOOH phases. The mixture consisted of ~40 wt.% α-Fe_2O_3 and ~60 wt.% α-FeOOH. Indeed, slowing down the rate of the phase transformation from goethite to hematite induced by the CTAB addition followed a similar fashion as for the sample S1. Furthermore, the synthesis of samples RS3, S7, and S3 showed that the addition of CTAB did not affect the goethite-to-hematite transformation (see Figures 4 and 6). In these samples, single-phase α-Fe_2O_3 precipitated in the nanometer range, as unraveled from the PXRD line-broadening analysis.

Atyam et al. [88] described that the IR peaks at 536 and 468 cm^{-1} corresponded to Fe-O bonding of iron oxide for well-calcined particles appearing with the increase of temperature, which was in excellent agreement with our study, as we can see the shift of the IR band (Figure 1) compared to the samples prepared at 150 °C (sample S1) and those prepared at 200 or 250 °C (samples S2 and S3). The FE-SEM analysis revealed that the goethite particles in samples RS1, S1, and S2 were nanorods and the hematite particles in all samples had irregular shapes and sizes in the range from ~10 nm to 1 μm.

As mentioned in the Introduction, the microwave-assisted synthesis ensured a quick investigation of the influence of various additives and their addition amount in the synthesis mixture. In particular, the samples precipitated at 200 °C for 20 min, but with different addition levels of CTAB in the precipitated system, from 0.25% in sample S4 to 2.5% in sample S6 (Figure 5). The addition of less than 0.25% CTAB had no significant effect on the goethite-to-hematite transformation process. However, higher additions of CTAB, from 0.5% to 2.5%, according to Table 2, indicated that as the amount of CTAB in the precipitated

mixture of samples increased, the composition of goethite and hematite varied, resulting in a smaller mass fraction of hematite phase in the final product. According to FE-SEM images of samples RS3, S3, and S7 and results of PXRD line-broadening analysis, it was concluded that CTAB addition had an insignificant influence on the size and shape of hematite particles.

Based on this rapid and straightforward iron oxide preparation method, future studies will investigate the effects of other surfactants: anionic, cationic, or nonionic on the precipitated mixture, with a strong emphasis placed on the reproducibility of the synthesis data produced by microwave technology.

5. Conclusions

In this work, we reported the facile and fast microwave-assisted hydrothermal synthesis of α-Fe_2O_3 particles from $FeCl_3$ solution in highly alkaline media by heating at 200 °C and 250 °C for 20 min. In these synthesis routes for hematite particles, it was proven that 0.25% of added CTAB slows down the transformation of goethite-to-hematite at 200 °C, but any percentage of added CTAB had no effect on transformation at 250 °C. The shape of the synthesized particles, goethite nanorods, and irregular hematite was about a few tens of nm to 1 μm in size regardless of temperature or CTAB addition.

Author Contributions: Methodology, L.G. and A.P. (Andrea Paut); validation, I.M., Ž.S., and M.V.; formal analysis, I.M., Ž.S., and M.V.; investigation, I.M. and S.K.; resources, I.M.; data curation, I.M.; writing—original draft preparation, I.M.; writing—review and editing, I.M., L.G., A.P. (Andrea Paut), M.V., and S.K.; visualization, I.M. and M.V.; supervision, I.M.; project administration, A.P. (Ante Prkić) and S.K.; funding acquisition, I.M., A.P. (Ante Prkić), and S.K. All authors have read and agreed to the published version of the manuscript.

Funding: This work was funded by Croatian Science Foundation, project numbers: UIP-2017-05-6282 and IP-2016-06-8254.

Data Availability Statement: Not applicable.

Conflicts of Interest: The authors declare no conflict of interest.

References

1. Bilecka, I.; Niederberger, M. Microwave chemistry for inorganic nanomaterials synthesis. *Nanoscale* **2010**, *2*, 1358–1374. [CrossRef]
2. Kappe, C.O. How to measure reaction temperature in microwave-heated transformations. *Chem. Soc. Rev.* **2013**, *42*, 4977–4990. [CrossRef] [PubMed]
3. Van der Eycken, E.V. Practical Microwave Synthesis for Organic Chemists.Strategies, Instruments, and Protocols. Edited by C. Oliver Kappe, Doris Dallinger and Shaun Murphree. *Angew. Chem. Int. Ed.* **2009**, *48*, 2828–2829. [CrossRef]
4. Schutz, M.B.; Xiao, L.S.; Lehnen, T.; Fischer, T.; Mathur, S. Microwave-assisted synthesis of nanocrystalline binary and ternary metal oxides. *Int. Mater. Rev.* **2018**, *63*, 341–374. [CrossRef]
5. Nüchter, M.; Ondruschka, B.; Bonrath, W.; Gum, A. Microwave assisted synthesis–a critical technology overview. *Green Chem.* **2004**, *6*, 128–141. [CrossRef]
6. Cornell, R.M.; Schwertmann, U. *The Iron Oxides: Structure, Properties, Reactions, Occurrence, and Uses*; VCH: New York, NY, USA, 2003.
7. Buxbaum, G. *Industrial Inorganic Pigments*, 1st ed.; VCH: New York, NY, USA, 1993; p. 281.
8. Li, P.; Miser, D.; Rabiei, S.; Yadav, R.; Hajaligol, M. The removal of carbon monoxide by iron oxide nanoparticles. *Appl. Catal. B* **2003**, *43*, 151–162. [CrossRef]
9. Zhang, W.; Singh, P.; Paling, E.; Delides, S. Arsenic removal from contaminated water by natural iron ores. *Miner. Eng.* **2004**, *17*, 517–524. [CrossRef]
10. Mohapatra, M.; Anand, S. Synthesis and applications of nano-structured iron oxides or hidroxides—A review. *Int. J. Eng. Sci. Technol.* **2010**, *2*, 127–146.
11. Lu, A.-H.; Salabas, E.L.; Schueth, F. Magnetic nanoparticles: Synthesis, protection, functionalization, and application. *Angew. Chem. Int. Ed.* **2007**, *46*, 1222–1244. [CrossRef] [PubMed]
12. Marinho, J.Z.; Montes, R.H.O.; de Moura, A.P.; Longo, E.; Varela, J.A.; Munoz, R.A.A.; Lima, R.C. Rapid preparation of alpha-FeOOH and alpha-Fe2O3 nanostructures by microwave heating and their application in electrochemical sensors. *Mater. Res. Bull.* **2014**, *49*, 572–576. [CrossRef]
13. Prkić, A.; Vukušić, T.; Mitar, I.; Giljanović, J.; Sokol, V.; Bošković, P.; Jakić, M.; Sedlar, A. New sensor based on AgCl containing Iron Oxide or Zinc Oxide Nanoparticles for Chloride Determination. *Int. J. Electrochem. Sci* **2019**, *14*, 861–874. [CrossRef]
14. Schwertmann, U.; Cornell, R.M. *Iron Oxides in the Laboratory: Preparation and Characterization*; VCH: New York, NY, USA, 2000; p. 204.

15. Wang, J.; Zhang, K.; Peng, Z.M.; Chen, Q.W. Magnetic properties improvement in Fe_3O_4 nanoparticles grown under magnetic fields. *J. Cryst. Growth* **2004**, *266*, 500–504. [CrossRef]
16. Akbarzadeh, A.; Samiei, M.; Davaran, S. Magnetic nanoparticles: Preparation, physical properties, and applications in biomedicine. *Nanoscale Res. Lett.* **2012**, *7*, 144–157. [CrossRef] [PubMed]
17. Laurent, S.; Forge, D.; Port, M.; Roch, A.; Robic, C.; Elst, L.; Muller, R. Magnetic iron oxide nanoparticles: Synthesis, stabilization, vectorization, physicochemical characterizations, and biological applications. *Chem. Rev.* **2008**, *108*, 2064–2110. [CrossRef] [PubMed]
18. Yue, J.; Jiang, X.; Kaneti, Y.V.; Yu, A. Experimental and theoretical study of low-dimensional iron oxide nanostructures. In *Smart Nanoparticles Technology*; InTech: London, UK, 2012; pp. 119–146.
19. Machala, L.; Tucek, J.; Zboril, R. Polymorphous transformations of nanometric iron(III) oxide—A review. *Chem. Mater.* **2011**, *23*, 3255–3272. [CrossRef]
20. Wu, W.; He, Q.; Jiang, C. Magnetic iron oxide nanoparticles: Synthesis and surface functionalization strategies. *Nanoscale Res. Lett.* **2008**, *3*, 397–415. [CrossRef] [PubMed]
21. Teja, A.S.; Koh, P.-Y. Synthesis, properties, and applications of magnetic iron oxide nanoparticles. *Prog. Cryst. Growth Charact. Mater.* **2009**, *55*, 22–45. [CrossRef]
22. Žic, M.; Ristić, M.; Musić, S. Fe^{57} Mössbauer, FT-IR and FE SEM investigation of the formation of hematite and goethite at high pH values. *J. Mol. Struct.* **2007**, *834*, 141–149. [CrossRef]
23. Gotić, M.; Popović, S.; Ljubešić, N.; Musić, S. Structural Properties of Precipitates Formed by Hydrolysis of Fe3+ Ions in Aqueous Solutions Containing NO3- and Cl- Ions. *J. Mater Sci.* **1994**, *29*, 2474–2480. [CrossRef]
24. Musić, S.; Vertes, A.; Simmons, G.W.; Czakonagy, I.; Leidheiser, H. Mössbauer spectroscopic study of the formation of Fe(III) oxyhydroxides and oxides by hydrolysis of aqueous Fe(III) salt-solutions. *J. Colloid Interface Sci.* **1982**, *85*, 256–266. [CrossRef]
25. Šarić, A.; Musić, S.; Nomura, K.; Popović, S. Microstructural properties of Fe-oxide powders obtained by precipitation from $FeCl_3$ solutions. *Mater. Sci. Eng. B* **1998**, *56*, 43–52. [CrossRef]
26. Musić, S.; Santana, G.P.; Smit, G.; Garg, V.K. Fe^{57} Mössbauer, FT-IR and TEM investigations of Fe-oxide powders obtained from concentrated $FeCl_3$ solutions. *J. Alloys Compd.* **1998**, *278*, 291–301. [CrossRef]
27. Musić, S.; Maljković, M.; Popović, S. Chemical and microstructural properties of iron oxide powders obtained from $FeCl_3$ solutions with decomposing urea. *ACH Models Chem.* **1999**, *136*, 299–316.
28. Musić, S.; Krehula, S.; Popović, S.; Skoko, Z. Some factors influencing forced hydrolysis of $FeCl_3$ solutions. *Mater. Lett.* **2003**, *57*, 1096–1102. [CrossRef]
29. Musić, S.; Krehula, S.; Popović, S. Effect of HCl additions on forced hydrolysis of $FeCl_3$ solutions. *Mater. Lett.* **2004**, *58*, 2640–2645. [CrossRef]
30. Krehula, S.; Music, S. Influence of ruthenium ions on the precipitation of α-FeOOH, α-Fe_2O_3 and Fe_3O_4 in highly alkaline media. *J. Alloys Compd.* **2006**, *416*, 284–290. [CrossRef]
31. Ristić, M.; Musić, S.; Godec, M. Properties of γ-FeOOH, α-FeOOH and α-Fe_2O_3 particles precipitated by hydrolysis of Fe^{3+} ions in perchlorate containing aqueous solutions. *J. Alloys Compd.* **2006**, *417*, 292–299. [CrossRef]
32. Gotić, M.; Musić, S. Mössbauer, FT-IR and FE SEM investigation of iron oxides precipitated from $FeSO_4$ solutions. *J. Mol. Struct.* **2007**, *834*, 445–453. [CrossRef]
33. Krehula, S.; Musić, S. Influence of aging in an alkaline medium on the microstructural properties of α-FeOOH. *J. Cryst. Growth* **2008**, *310*, 513–520. [CrossRef]
34. Žic, M.; Ristić, M.; Musić, S. Microstructural changes in particles detected during the transformation from β-FeOOH to α-Fe_2O_3 in dense aqueous suspensions. *J. Alloys Compd.* **2008**, *464*, 81–88. [CrossRef]
35. Gotić, M.; Musić, S.; Popović, S.; Sekovanić, L. Investigation of factors influencing the precipitation of iron oxides from Fe(II) containing solutions. *Croat. Chem. Acta* **2008**, *81*, 569–578.
36. Žic, M.; Ristić, M.; Musić, S. Precipitation of α-Fe_2O_3 from dense β-FeOOH suspensions with added ammonium amidosulfonate. *J. Mol. Struct.* **2009**, *924–926*, 235–242. [CrossRef]
37. Žic, M.; Ristić, M.; Musić, S. The effect of temperature on the crystallization of α-Fe_2O_3 particles from dense β-FeOOH suspensions. *Mater. Chem. Phys.* **2010**, *120*, 160–166. [CrossRef]
38. Opačak, I.; Ristić, M.; Musić, S. Preparation and characterization of hollow alpha-Fe2O3 irregular microspheres. *Mater. Lett.* **2010**, *64*, 2555–2558. [CrossRef]
39. Žic, M.; Ristić, M.; Musić, S. Monitoring the hydrothermal precipitation of α-Fe_2O_3 from concentrated $Fe(NO_3)_3$ solutions partially neutralized with NaOH. *J. Mol. Struct.* **2011**, *993*, 115–119. [CrossRef]
40. Ristić, M.; Opačak, I.; Musić, S. The synthesis and microstructure of goethite particles precipitated in highly alkaline media. *J. Alloys Compd.* **2013**, *559*, 49–56. [CrossRef]
41. Ristić, M.; Fujii, T.; Hashimoto, H.; Opačak, I.; Musić, S. A novel route in the synthesis of magnetite nanoparticles. *Mater. Lett.* **2013**, *100*, 93–97. [CrossRef]
42. Ristić, M.; Štajdohar, J.; Mitar, I.; Musić, S. Monitoring of the Forced Hydrolysis of FeCl3 Solutions in the Presence of Sodium Dodecyl Sulphate. *Croat. Chem. Acta* **2018**, *91*, 403–410. [CrossRef]
43. Ristić, M.; Mitar, I.; Musić, S. Forced hydrolysis of FeCl3 solutions in the presence of sodium dextran sulphate. *Colloid Polym. Sci.* **2019**, *297*, 177–182. [CrossRef]

44. Gupta, A.K.; Gupta, M. Synthesis and surface engineering of iron oxide nanoparticles for biomedical applications. *Biomaterials* **2005**, *26*, 3995–4021. [CrossRef]
45. Wu, W.; Jiang, C.Z.; Roy, V.A.L. Designed synthesis and surface engineering strategies of magnetic iron oxide nanoparticles for biomedical applications. *Nanoscale* **2016**, *8*, 19421–19474. [CrossRef] [PubMed]
46. Faraji, M.; Yamini, Y.; Rezaee, M. Magnetic nanoparticles: Synthesis, stabilization, functionalization, characterization, and applications. *J. Iran. Chem. Soc.* **2010**, *7*, 1–37. [CrossRef]
47. Wang, W.; Zhu, Y.; Ruan, M. Microwave assisted synthesis and magnetic property of magnetite and hematite nanoparticles. *J. Nanopart. Res.* **2007**, *9*, 419–426. [CrossRef]
48. Hu, L.; Percheron, A.; Chaumont, D.; Brachais, C.H. Microwave-assisted one-step hydrothermal synthesis of pure iron oxide nanoparticles: Magnetite, maghemite and hematite. *J. Sol Gel Sci. Technol.* **2011**, *60*, 198–205. [CrossRef]
49. Jiang, F.; Wang, C.; Fu, Y.; Liu, R. Synthesis of iron oxide nanocubes via microwave assisted solvolthermal method. *J. Alloys Compd.* **2010**, *503*, 31–33. [CrossRef]
50. Yin, S.; Luo, Z.; Xia, J.; Li, H. Microwave-assisted synthesis of Fe3O4 nanorods and nanowires in an ionic liquid. *J. Phys. Chem. Solids* **2010**, *71*, 1785–1788. [CrossRef]
51. Cao, S.-W.; Zhu, Y.-J. Iron oxide hollow spheres: Microwave–hydrothermal ionic liquid preparation, formation mechanism, crystal phase and morphology control and properties. *Acta Mater.* **2009**, *57*, 2154–2165. [CrossRef]
52. Xavier, C.S.; Paskocimas, C.A.; da Motta, F.V.; Araujo, V.D.; Aragon, M.J.; Tirado, J.L.; Lavela, P.; Longo, E.; Delmonte, M.R.B. Microwave-assisted Hydrothermal Synthesis of Magnetite Nanoparticles with Potential Use as Anode in Lithium Ion Batteries. *Mater. Res.* **2014**, *17*, 1065–1070. [CrossRef]
53. Osborne, E.A.; Atkins, T.M.; Gilbert, D.A.; Kauzlarich, S.M.; Liu, K.; Louie, A.Y. Rapid microwave assisted synthesis of dextran coated iron oxide nanoparticles for magnetic resonance imaging. *Nanotechnology* **2012**, *23*, 3461–3467. [CrossRef]
54. Komarneni, S.; D'Arrigo, M.C.; Leonelli, C.; Pellacani, G.C.; Katsuki, H. Microwave-hydrothermal synthesis of nanophase ferrites. *J. Am. Ceram. Soc.* **1998**, *81*, 3041–3043. [CrossRef]
55. Sreeja, V.; Joy, P. Microwave hydrothermal synthesis of γ-Fe_2O_3 nanoparticles and their magnetic properties. *Mater. Res. Bull.* **2007**, *42*, 1570–1576. [CrossRef]
56. Katsuki, H.; Komarneni, S. Microwave-Hydrothermal Synthesis of Monodispersed Nanophase α-Fe2O3. *J. Am. Ceram. Soc.* **2001**, *84*, 2313–2317. [CrossRef]
57. Ni, H.; Ni, Y.; Zhou, Y.; Hong, J. Microwave–hydrothermal synthesis, characterization and properties of rice-like α-Fe2O3 nanorods. *Mater. Lett.* **2012**, *73*, 206–208. [CrossRef]
58. Khollam, Y.B.; Dhage, S.R.; Potdar, H.S.; Deshpande, S.B.; Bakare, P.P.; Kulkarni, S.D.; Date, S.K. Microwave hydrothermal preparation of submicron-sized spherical magnetite (Fe3O4) powders. *Mater. Lett.* **2002**, *56*, 571–577. [CrossRef]
59. Bakare, P.P.; Date, S.K.; Khollam, Y.B.; Deshpande, S.B.; Potdar, H.S.; Salunke-Gawali, S.; Varret, F.; Pereira, E. Mössbauer effect studies on the formation of iron oxide phases synthesized via microwave–hydrothermal route. *Hyperfine Interact.* **2006**, *168*, 1127–1132. [CrossRef]
60. Dhage, S.R.; Khollam, Y.B.; Potdar, H.S.; Deshpande, S.B.; Bakare, P.P.; Sainkar, S.R.; Date, S.K. Effect of variation of molar ratio (pH) on the crystallization of iron oxide phases in microwave hydrothermal synthesis. *Mater. Lett.* **2002**, *57*, 457–462. [CrossRef]
61. Parsons, J.; Luna, C.; Botez, C.; Elizalde, J.; Gardea-Torresdey, J. Microwave assisted synthesis of iron(III) oxyhydroxides/oxides characterized using transmission electron microscopy, X-ray diffraction, and X-ray absorption spectroscopy. *J. Phys. Chem. Solids* **2009**, *70*, 555–560. [CrossRef] [PubMed]
62. Hu, X.L.; Yu, J.C.; Gong, J.M. Fast production of self-assembled hierarchical alpha-Fe2O3 nanoarchitectures. *J. Phys. Chem. C* **2007**, *111*, 11180–11185. [CrossRef]
63. Mahmoud, W.E.; Al-Hazmi, F.; Al-Noaiser, F.; Al-Ghamdi, A.A.; Bronstein, L.M. A facile method to syntheses monodisperse gamma-Fe2O3 nanocubes with high magnetic anisotropy density. *Superlattices Microstruct.* **2014**, *68*, 1–5. [CrossRef]
64. Deshmukh, R.G.; Badadhe, S.S.; Mulla, I.S. Microwave-assisted synthesis and humidity sensing of nanostructured alpha-Fe2O3. *Mater. Res. Bull.* **2009**, *44*, 1179–1182. [CrossRef]
65. Dias, A.M.G.C.; Hussain, A.; Marcos, A.S.; Roque, A.C.A. A biotechnological perspective on the application of iron oxide magnetic colloids modified with polysaccharides. *Biotechnol. Adv.* **2011**, *29*, 142–155. [CrossRef]
66. Ngenefeme, F.-T.J.; Eko, N.J.; Mbom, Y.D.; Tantoh, N.D.; Rui, K.W.M. A one pot green synthesis and characterisation of iron oxide pectin hybrid nanocomposite. *Open J. Compos. Mater.* **2013**, *3*, 30–37. [CrossRef]
67. Kim, D.K.; Zhang, Y.; Voit, W.; Rao, K.V.; Muhammed, M. Synthesis and characterization of surfactant-coated superparamagnetic monodispersed iron oxide nanoparticles. *J. Magn. Magn. Mater.* **2001**, *225*, 30–36. [CrossRef]
68. Shokuhfar, A.; Alibeigi, S.; Vaezi, M.R.; Sadrnezhaad, S.K. Synthesis of Fe3O4 Nanoparticles Prepared by Various Surfactants and Studying their Characterizations. *Defect Diffus. Forum.* **2008**, *273–276*, 22–27.
69. Ristić, M.; Kuzmann, E.; Homonnay, Z.; Mitar, I.; Musić, S. Hydrolysis of Fe(III) in the presence of mixed anions and promoters. *J. Radioanal. Nucl. Chem.* **2020**, *324*, 1293–1302. [CrossRef]
70. Ristić, M.; Opačak, I.; Stajdohar, J.; Musić, S. The influence of CTAB and gum arabic on the precipitation of alpha-FeOOH in a highly alkaline medium. *J. Mol. Struct.* **2015**, *1090*, 129–137. [CrossRef]
71. Ristić, M.; Štajdohar, J.; Opačak, I.; Musić, S. The Effect of Sodium Dodecyl Sulphate On The Forced Hydrolysis Of FeCl3 Solutions. *Contrib. Sect. Nat. Math. Biotech. Sci.* **2017**, *38*, 57–67. [CrossRef]

72. Yue, J.; Jiang, X.; Zeng, Q.; Yu, A. Experimental and numerical study of cetyltrimethylammonium bromide (CTAB)-directed synthesis of goethite nanorods. *Solid State Sci.* **2010**, *12*, 1152–1159. [CrossRef]
73. Karami, H.; Chidar, E. Pulsed-Electrochemical Synthesis and Characterizations of Magnetite Nanorods. *Int. J. Electrochem Sci.* **2012**, *7*, 2077–2090.
74. Williams, D.N.; Gold, K.A.; Holoman, T.R.P.; Ehrman, S.H.; Wilson, O.C., Jr. Surface modification of magnetic nanoparticles using gum arabic. *J. Nanopart. Res.* **2006**, *8*, 749–753. [CrossRef]
75. Wu, C.-C.; Chen, D.-H. Facile green synthesis of gold nanoparticles with gum arabic as a stabilizing agent and reducing agent. *Gold Bull.* **2010**, *43*, 234–240. [CrossRef]
76. Yang, C.-Y.; Cheng, M.-F.; Tsai, S.-S.; Hung, C.-F. Fluoride in Drinking Water and Cancer Mortality in Taiwan. *Environ. Res.* **2000**, *82*, 189–193. [CrossRef] [PubMed]
77. Cole, A.J.; David, A.E.; Wang, J.; Galban, C.J.; Hill, H.L.; Yang, V.C. Polyethylene glycol modified, cross-linked starch coated iron oxide nanoparticles for enhanced magnetic tumor targeting. *Biomaterials* **2011**, *32*, 2183–2193. [CrossRef] [PubMed]
78. Kumagai, M.; Imai, Y.; Nakamura, T.; Yamasaki, Y.; Sekino, M.; Ueno, S.; Hanaoka, K.; Kikuchi, K.; Nagano, T.; Kaneko, E.; et al. Iron hydroxide nanoparticles coated with poly(ethylene glycol)-poly(aspartic acid) block copolymer as novel magnetic resonance contrast agents for in vivo cancer imaging. *Colloids Surf. B* **2007**, *56*, 174–181. [CrossRef] [PubMed]
79. Yang, D.P.; Gao, F.; Cui, D.X.; Yang, M. Microwave Rapid Synthesis of Nanoporous Fe3O4 Magnetic Microspheres. *Curr. Nanosci.* **2009**, *5*, 485–488. [CrossRef]
80. *Origin 2020b*; OriginLab Corporation: Northampton, MA, USA, 2020.
81. Unlu, C.G.; Kaynar, M.B.; Simsek, T.; Tekgul, A.; Kalkan, B.; Ozcan, S. Structure and magnetic properties of (La1-xFex)FeO3(x = 0, 0.25, 0.50) perovskite. *J. Alloy. Compd.* **2019**, *784*, 1198–1204. [CrossRef]
82. Rietveld, H. A profile refinement method for nuclear and magnetic structures. *J. Appl. Crystallogr.* **1969**, *2*, 65–71. [CrossRef]
83. *HighScore Plus Program, Version 4.1*; PANalytical: Almelo, The Netherlands, 2014.
84. Cambier, P. Infrared study of goethites of varying crystallinity and particle size 1: Interpretation of OH and lattice vibration frequencies. *Clay Miner.* **1986**, *21*, 191–200. [CrossRef]
85. Wang, Y.S.; Muramatsu, A.; Sugimoto, T. FTIR analysis of well defined α-Fe_2O_3 particles. *Colloids Surf. A* **1998**, *134*, 281–297. [CrossRef]
86. Hill, R.J.; Howard, C.J. Quantitative phase analysis from neutron powder diffraction data using the Rietveld method. *J. Appl. Crystallogr.* **1987**, *20*, 467–474. [CrossRef]
87. Young, R.A.; Prince, E.; Sparks, R.A. Suggested guidelines for the publication of Rietveld analyses and pattern decomposition studies. *J. Appl. Crystallogr.* **1982**, *15*, 357–359. [CrossRef]
88. Atyam, K.K.; Ghosh, A.; Mukherjee, K.; Majumder, S.B. Hematite iron oxide nano-particles: Facile synthesis and their chemi-resistive response towards hydrogen. *Mater. Res. Express* **2015**, *2*, 7. [CrossRef]